Retrospective PET/CT Imaged Based Dosimetry Following Transarterial Radioembolization

Briana C. Thompson (brthomps@wakehealth.edu)
Wake Forest University School of Medicine https://orcid.org/0000-0002-4691-3628
William A. Dezarn
Wake Forest Baptist Medical Center

Original research

Keywords: Y-90 PET/CT, Radioembolization, dose distribution, imaged based dosimetry

Posted Date: September 10th, 2020

DOI: https://doi.org/10.21203/rs.3.rs-68826/v1

Abstract

Background: Transarterial Radioembolization (TARE) uses beta particle emitting microspheres, containing Yttrium 90 (^{90}Y), to treat unresectable primary and metastatic liver tumors. Current dosimetry models are highly simplistic. ^{90}Y post-TARE PET/CT images are being evaluated for their use in image based dosimetry post treatment allowing for improved treatment efficacy. We sought to provide guidance on reconstruction and dose calculation algorithms that give the most reliable image based dosimetry.

Methods: Retrospective image study for 11 patients each having a ^{90}Y PET/CT following TARE SIR-Spheres® treatment. In total, 6 emission images were reconstructed using Ordered Subset Expectation Maximization (OSEM) routines and Bayesian penalized-likelihood reconstruction algorithms (Q. Clear). PET/CT image sets were resampled to 3mm resolution and used to create voxel based dose distributions using our own convolution algorithm (WFBH), SurePlan™ MIRD and SurePlan™ LDM. Additionally, we analyzed the effects of a systematic personalized background subtraction prior to dose distribution creation.

Results: Reconstructed activity was highest among Q. Clear β = 350 and 1000 and both OSEM methods. OSEM with 3 iterations and 24 subsets gave comparable dose distributions to Q. Clear β=1000 (max dose ratio of 0.96 ± 0.14). No statistical difference was identified among Q. Clear and OSEM methods comparing dose distributions with and without additional background subtraction post-reconstruction (average local gamma value = 98.01% ± 3.75%). LDM is more sensitive than MIRD to small activity differences between reconstruction methods (p-value= 0.048). LDM calculated max dose values were higher than MIRD. DVH curves showed LDM model potentially underestimates low dose values and overestimates high dose values.

Conclusion: Background subtraction is sufficiently addressed in PET image reconstruction. We recommend post-TARE image based dosimetry to be calculated using image series reconstructed with Q. Clear β= 1000 or OSEM 3 iterations 24 subsets and using a convolution voxel based dose algorithm, such as SurePlan™ MIRD. Since more sophisticated corrections are not available at present, the ^{90}Y activity distribution should be scaled by the local clinic's activity recovery fraction, which also will directly scale the calculated dose distribution.

Background

Transarterial Radioembolization (TARE) is a treatment modality for unresectable primary and metastatic liver tumors where beta particle emitting microspheres are injected locally to implant around the tumor(s). TARE treatment typically utilizes the hepatic artery as a passageway to deliver Yttrium-90 (^{90}Y) containing microspheres that have a maximum radiation delivery range of 11 mm and a mean range of 2.5 mm in tissue [1–3]. Prior to treatment, Technetium-99m macroaggregated albumin particles (^{99m}Tc-MAA) are used as a predictor of ^{90}Y microsphere distribution and are assumed to be a valid foundation for dosimetry calculations [1, 4–6]. However, due to the complexity of this treatment modality there is

often poor agreement in distribution between ^{99m}Tc-MAA particles and ^{90}Y microspheres upon treatment[7–9]. Following the dosimetry process for general brachytherapy procedures, post-TARE emission imaging validation is necessary for patient safety and accurate measures of absorbed dose [7–11].

The most common post-TARE imaging protocol is ^{90}Y bremsstrahlung single-photon emission computed tomography (SPECT) to verify treatment deposition in the liver along with no extrahepatic microsphere deposition [1, 12]. Due to the noisy nature of these images, they are typically used only for qualitative purposes because quantitative assessment is difficult[1, 13]. However, many institutions have been looking at the promising option of post-TARE ^{90}Y positron emission tomography (PET) imaging. Although a majority (99.983%) of ^{90}Y decays through beta minus decay to the ground sate of Zirconium-90 (^{90}Zr), there is a small decay branch that decays to the 0^+ first excited state of ^{90}Zr at 1760 keV; which is followed by an internal pair production with a branching ratio of $(32.6 \pm 0.07) \times 10^{-6}$ [1, 14–16]. This small positron emission allows for the use of PET imaging post-TARE as an option for quantification of radioactivity within the treated region and improved spatial resolution compared to bremsstrahlung SPECT [13, 17–19]. Additionally, from a clinical perspective, these post-TARE ^{90}Y PET images give an evaluation of a treatment's technical success as well as allow generation of absorbed dose maps which have the potential to predict treatment efficacy [5, 20, 21]. Furthermore, they can provide a management plan for patient follow-up as well as treatment-planning for successive therapies [21, 22]. Others have reported variation amongst reconstruction methods but there is strong evidence to suggest that these ^{90}Y PET images are accurate in their quantifiable data and therefore can be used as dosimetric tools once the necessary parameters are optimized [10, 17, 23]. This study aims to provide guidance on optimal reconstruction method and dose calculation algorithm for the most reliable image based dosimetry.

The two reconstruction methods explored are a Regularized Reconstruction iterative algorithm (Q.Clear) [24] and an Ordered Subsets Expectation Maximization (OSEM) algorithm. Q. Clear is a Bayesian penalized likelihood reconstruction algorithm with an additional term that allows it to reach full convergence, steering the optimization away from nosier images[24]. OSEM is an accelerated variant of the Maximum-Likelihood Expectation Maximization algorithm using an update equation to create a new image with increased likelihood while reducing reconstruction time by performing updates based on small parts of the data at once[24].

Materials And Methods

Two types of studies were executed in this work to understand post-TARE dosimetry effects based on reconstruction and dose calculation algorithms: phantom studies and patient studies.

Phantom based study

A phantom study using a National Electrical Manufacturers Association NU-2 image quality phantom was performed. A ^{90}Y PET/CT image was initially acquired on a GE Discovery MI DR™ (GE Healthcare, Chicago, IL, USA) system with a scan time of 5 minutes per bed position on day 0, with an increase in acquisition time to 10 minutes and 20 minutes on day 4 and 7 respectively, in order to keep total counts consistent across time points as we account for decay. Six different reconstructed ^{90}Y PET image series were analyzed for each day: four Q. Clear variations with β parameter values of 350, 1000, 4000 and 7000 and two OSEM variations using 3 iterations and 18 or 24 subsets. This set of PET images were reconstructed at the time of image acquisition on the scanner with a slice thickness of 3.27 mm and pixel spacing of 2.73 mm x 2.73 mm. Each emission image was then retrospectively resampled to 3 mm cubic voxels and analyzed, both using MIM Software SurePlan™ (MIM Software Inc., Cleveland, OH). Each sphere within the phantom was contoured on its associated CT image and the contours were then transferred to each reconstructed PET image. The sphere sizes within the phantom have the following diameters: 10 mm, 13 mm, 17 mm, 22 mm, 28 mm and 37 mm. Recovered activity (RA) values for each sphere was calculated using the equation below where $\bar{p}$ is the mean pixel value in the volume of interest (VOI) and c is the known activity concentration.

$$RA = \frac{\bar{p}}{c}$$

Additionally, dose distributions based on these images were created using multiple algorithms.

Patient based study

We followed an IRB approved retrospective patient imaging review in which post-TARE image based dosimetry models were created for 11 patients who underwent treatment at Wake Forest Baptist Medical Center between July 2016 – March 2018 (Table 1 shows patient characteristics). All patients consented to a positron emission tomography/computed tomography (PET/CT) within 4 hours of treatment acquired on a GE Discovery MI DR™ (GE Healthcare, Chicago, IL, USA) system following SIR-Spheres® (Sirtex SIR-Spheres Pty Ltd., St Leonards, Australia) implantation in addition to the standard protocol of a Philips Healthcare™ bremsstrahlung single photon emission computed tomography/computed tomography (SPECT/CT). Emission scans were reconstructed using the same six algorithms described above in the phantom based study and resampled SurePlan™ to 3 mm cubic voxel size.

Table 1
Patient characteristics for those included in this study

Patient Number	Sex	Lung Shunt	Treated Volume	Liver (cm^3)	Tumor (cm^3)	SMAC Activity (GBq)	Activity Delivered (GBq)
1	female	2.4%	Rt Lobe	2065.7	521.4	1.07	1.07
2	female	3.3%	Seg 4	2109.5	73.4	0.25	0.25
3	male	4.1%	Rt Lobe	2758.3	209.8	1.46	1.55
4	male	6.5%	Rt Lobe	1839.8	73.0	1.00	1.05
5	female	1.1%	Rt Lobe	1880.3	478.5	1.37	1.39
6	female	5.1%	Rt Lobe	1756.8	204.6	1.60	1.70
7	male	3.6%	Rt Lobe	2212.9	304.2	0.97	1.01
8	female	2.8%	Rt Lobe	1990.7	139.0	0.90	0.93
9	female	2.4%	Rt Lobe	2741.2	690.7	1.25	1.14
10	female	1.5%	Lt Lobe	1972.8	218.6	0.90	0.95
11	male	17.7%	Lt Lobe	2649.3	692.2	1.01	1.04

Dose distributions were created for each ^{90}Y PET image series using SurePlan™ Local Deposition Method (LDM), SurePlan™ Medical Internal Radiation Dose using voxel S values (MIRD), and our own dose convolution algorithm using voxel S values (WFBH). Figure 1 shows an example of these image based dosimetry models. Methods to compare dose distributions include local gamma analysis, dose profiles taken along a sagittal line through the max dose point defined by the dose distribution created using MIRD Q. Clear 1000 and dose volume histogram (DVH) curve comparison.

To study the effects of background on post-TARE dosimetry, a CT contour defined as the whole body minus the liver and lungs expanded by 2 cm was created. Figure 2 is a representative background contour shaded in blue. The average concentration of activity found in this contour was taken as the constant background value (Table 2 shows average statistics for this contour over all patients*)* for each corresponding image set and a dose distribution with this value subtracted was created using our WFBH dose algorithm (WFBH Bkgrd).

Table 2
Background contour statistics based on reconstruction method

		Average over all patients	SD over all patients
Q. Clear 350	Average activity in Bkgrd contour (BQML)	13836.30	13026.86
	Maximum activity in Bkgrd contour (BQML)	33140367.36	44605902.69
	SD activity in Bkgrd contour (BQML)	215803.70	232817.96
Q. Clear 1000	Average activity in Bkgrd contour (BQML)	11147.37	7530.93
	Maximum activity in Bkgrd contour (BQML)	22703045.82	24818314.24
	SD activity in Bkgrd contour (BQML)	150395.37	127327.51
Q. Clear 4000	Average activity in Bkgrd contour (BQML)	7649.39	3792.28
	Maximum activity in Bkgrd contour (BQML)	6017634.33	3678813.93
	SD activity in Bkgrd contour (BQML)	39154.04	18979.25
Q. Clear 7000	Average activity in Bkgrd contour (BQML)	6732.98	2817.15
	Maximum activity in Bkgrd contour (BQML)	1484059.17	996163.48
	SD activity in Bkgrd contour (BQML)	19531.11	9336.47
OSEM 18	Average activity in Bkgrd contour (BQML)	9674.23	7942.94
	Maximum activity in Bkgrd contour (BQML)	6675826.41	8697105.77
	SD activity in Bkgrd contour (BQML)	65146.66	63902.11
OSEM 24	Average activity in Bkgrd contour (BQML)	7802.49	6377.28
	Maximum activity in Bkgrd contour (BQML)	7204813.14	7323991.14
	SD activity in Bkgrd contour (BQML)	65801.33	49033.50

These background contour statistics are averaged over all patients in the study and are presented for each reconstruction method

Results

Shown in Fig. 3 are RA values measured for each image reconstruction series for the four larger sphere sizes in the phantom on Day 0. RA values of the 10 mm and 13 mm spheres are omitted from this figure due to their large uncertainty. With this data we investigated the effects of reconstruction method on RA to validate the accuracy of activity represented in these ^{90}Y PET images to better understand the reliability of activity in patient images. As sphere size decreased so did the calculated RA value which is due to the partial volume effect [10]. Table 3 shows the two-tailed paired p-values comparing the calculated RA for a given sphere size across reconstruction methods over the course of decay. RA values obtained through Q. Clear reconstruction methods with β values of 4000 and 7000 are statistically different and lower than those obtained via β values of 350 and 1000. There is no statistical difference in RA values obtained when comparing based on β values 350 and 1000. There are similar RA values within each sphere when the two OSEM reconstruction methods are compared to one another but moreover cannot make a conclusive statement on differences among Q. Clear methods and OSEM methods I reference to RA. Q.Clear 350 gives the largest RA values for all the spheres, denoting this reconstruction method to be the most accurate representation of activity compared to the known injected value. There is a significant loss in accuracy in the amount of activity recovered in each sphere when looking at Q. Clear 4000 and 7000. However, looking at OSEM methods there are comparable RA values to those obtained through Q. Clear 350 and 1000.

Table 3
Two-tailed paired p-values for RA based on sphere size and reconstruction method

β-value	sphere size (mm)	Q. Clear 1000	Q. Clear 4000	Q. Clear 7000	OSEM 18	OSEM 24
Q. Clear 350	**17**	0.053*	0.030*	0.022*	0.078*	0.002*
	22	0.103*	0.043*	0.027*	0.003*	0.048*
	28	0.061*	0.029*	0.021*	0.917*	0.119*
	37	0.068*	0.068*	0.012*	0.010*	0.001*
Q. Clear 1000	**17**		0.017*	0.011*	0.874*	0.461*
	22		0.015*	0.009*	0.203*	0.610*
	28		0.027*	0.018*	0.527*	0.453*
	37		0.006*	0.005*	0.438*	0.041*
Q. Clear 4000	**17**			0.007*	0.109*	0.172*
	22			0.005*	0.196*	0.303*
	28			0.010*	0.104*	0.005*
	37			0.004*	0.041*	0.148*
Q. Clear 7000	**17**				0.051*	0.072*
	22				0.064*	0.122*
	28				0.040*	0.003*
	37				0.018*	0.038*
OSEM 18	**17**					0.640*
	22					0.679*
	28					0.364*
	37					0.029*
*Denotes significance with a p-value less than 0.05						

The dosimetric effects of these reconstruction methods in patient post-TARE Y^{90} PET images with support from phantom studies is the focus of the study. Figure 4 shows a dose profile based on our phantom Y^{90} PET image comparing the different Q.Clear β values while dose calculation algorithm was held constant. Moreover, Fig. 5 shows a representative dose profile for our patient data. In both figures

you can see there is a smoothing effect within the dosimetry due to reduction in noise as β value increases which was quantitatively shown by Scott and McGowan[10].

Through comparable RA values and apparent noise reduction as beta values increase[10] there is no added value in using Q. Clear 350 over Q.Clear 1000 and only gives increased noise that effects resulting dosimetry in an unfavorable manner shown through the dose profiles in Figs. 4 and 5. There is a grouping of profiles in Fig. 5 based on Q. Clear 1000, OSEM 18 and OSEM 24 reconstruction methods showing spatial similarity but further analysis is necessary to determine absolute dose similarities.

Initially a complete analysis on all 6 reconstruction methods were performed for all of our patients. For the purposes of presenting data in a clear manner, we chose to present the data for the following four reconstruction methods: Q. Clear 1000, Q. Clear 4000, OSEM 18 and OSEM 24. Our rational behind these four methods was based on our phantom study results which eliminated Q.Clear 350 and Q.Clear 7000. Although Q. Clear 4000 appears to be inferior to Q.Clear 1000, it is included in our presented analysis due to Rowley et al. deeming it to be visually optimal[12].

A large problem with trying to use radioactive emission images for quantitative purposes is the effect of background noise on activity accuracy. We sought to understand the effects of background on dose distributions and how the various reconstruction methods handle this added noise that is patient specific. Overall, both Q. Clear and OSEM methods sufficiently handle background within their algorithms based on this study's definition of what was background activity. Figure 6 shows an example of the dose profiles comparing dose distributions with and without background subtraction for a representative patient. A two-tailed p-value for each patient comparing these dose profiles was calculated and showed no statistical difference between WFBH and WFBH Bkgrd dose distributions. Furthermore, Table 4 shows the local gamma analysis, which compares percent dose difference relative to the dose at the given point [25], values between WFBH and WFBH Bkgrd dose distributions with 3% dose difference at 3 mm distance with no low dose threshold. Gamma values had an average of 98.01% with standard deviation of 3.75%. Figure 7 then shows DVH curves for the liver contour and treated area for a representative patient. The treated area is defined to be the volume that has a dose value greater than 20% of the max dose. Overall, with both Q. Clear and OSEM reconstruction methods there was no significant effect on ^{90}Y PET based post-TARE dosimetry found when taking the additional step of background subtraction and therefore the reconstruction algorithms themselves handle this appropriately from the beginning.

Table 4
Local gamma analysis values between WFBH and WFBH Bkgrd dose distributions

patient no.	Q.Clear 1000	Q.Clear 4000	OSEM 18	OSEM 24
1	96.05	99.30	99.99	97.97
2	97.53	99.99	99.98	99.84
3	99.47	99.95	99.75	99.85
4	99.91	98.82	97.21	98.67
5	98.57	99.46	94.06	98.98
6	98.63	99.99	99.93	86.32
7	99.64	100.00	99.79	99.90
8	92.35	98.83	99.99	99.96
9	90.65	99.63	99.98	98.31
10	82.74	99.69	99.80	99.96
11	90.99	99.98	99.89	99.99

Comparing our WFBH convolution algorithm to the MIRD convolution algorithm through two tailed paired p-values of dose profiles and DVH curves, no statistical difference among WFBH and MIRD dose algorithms were found. Figure 8 shows representative DVH curves comparing MIRD and WFBH dose algorithms and their agreement. Note that the outlier sets of DVH curves are based on the Q. Clear 4000 reconstruction method.

Comparing LDM dose algorithm to MIRD for post-TARE ^{90}Y PET/CT patient images, LDM was statistically more dependent on reconstruction method than MIRD. For each patient the max dose obtained via LDM and MIRD for each reconstruction method was recorded and it was found that the standard deviation (SD) of the max dose values among the reconstruction methods were statistically higher (p-value = 0.048) within the LDM calculated values compared to the MIRD values. The spread of these deviations are shown in Fig. 9 and highlights how much the max dose fluctuates as a result of reconstruction method when using LDM. This same variance in max dose values based on reconstruction method was found in our phantom study with a SD between the reconstruction methods for LDM being 137.98 and MIRD being 52.51As detailed in Table 5, LDM is giving consistently higher dose values across the reconstruction methods when compared to their MIRD counterpart.

Table 5
Ratio of max dose value calculated by LDM to MIRD, averaged over all patients

	Q. Clear 1000	Q. Clear 4000	OSEM 18	OSEM 24
Average	1.987418	1.264204	1.224291	1.265757
Standard deviation	0.924286	0.466666	0.425819	0.392314

This overestimation of high dose regions is not just a scaling factor of the entire dose distribution as shown by the leftward shift in Fig. 10, where the percent of contour max is shown on the x-axis. If this were a scaling factor, then the DVH curves for the two dose algorithms would overlap with this renormalization to their respective max dose in place. However, instead we see that LDM algorithm derived dose distributions have a small percentage of volume with a high dose point thus there is a larger amount of lower dose values in comparison to MIRD derived dose distributions. Additionally, Fig. 11 plots absolute dose on the x-axis and shows that for higher dose values the LDM DVH curves cross over the MIRD DVH curves. Taking Figs. 10 and 11 together, the LDM model underestimates low dose values and over estimates high dose values. The variance in LDM dose estimation, along with the LDM sensitivity to reconstruction method, leads us to recommend the use of MIRD S Voxel algorithms for post-TARE ^{90}Y PET based dosimetry models.

Lastly, comparing our two OSEM reconstruction variations, the dose distributions for OSEM 18 and OSEM 24 are spatially comparable to the dose distributions based on our Q. Clear 1000 reconstruction algorithm. This is shown through dose profiles in Fig. 4 as well as DVH curves in Figs. 7–11. However, when looking at the max dose values in comparison to max dose values obtained via Q. Clear 1000, there is a statistical difference (p-value = 0.035) among the two groups with the average ratio to Q. Clear 1000 for OSEM 18 being 0.85 (SD = 0.15) and the average ratio for OSEM 24 being 0.96 (SD = 0.14) across all of our patients.

Discussion

Throughout our study we initially performed our analysis on all six reconstruction method variations. However, it became apparent to us that in combination with other's work [10, 12] we could focus the presentation of data better as we advanced in this study by eliminating the presentation of results for methods that were inferior. Scott and McGowan concluded based on phantom studies that the optimal β value for the Q.Clear reconstruction method for Y^{90} PET imaging was β = 1000[10]. Similar RA values were found to Scott and McGowan following the same trend of as β values increase, there is a decrease in RA; likely due to this parameter's involvement in noise suppression[10]. Initially, the potential of using Q. Clear β = 7000 reconstructed images for dosimetry purposes was eliminated due to its significantly lower RA values and overly smooth dose profiles. Next, in agreement with Scott and McGowan, Q. Clear β = 350 is less optimal than Q. Clear β = 1000 due to much larger dose gradients from neighboring voxels

for this reconstruction method, especially within low dose regions where less of this drastic variation is expected.

Moreover, all RA values are less than 0.80 for Y^{90} phantom sphere compartments. Typical fluorine-18 phantom studies give values that are much closer to unity across various imaging systems[26] and therefore the need for scaling is less of an issue with typical PET imaging. With these Y^{90} PET images however, we need to account for the loss of activity through scaling the image by the inverse of the measured RA. These phantom studies should be done alongside other annual QA calibration measurements in order to have site specific values and thus, most accurate rescaling values. At this time, we recommend using the RA value calculated for the 37 mm diameter sphere as the scaling factor seeing as its radius (18.5 mm) is larger than the maximum penetration depth of Y^{90} beta. In the future, more complex corrections are needed in order to account for RA changes as sphere size decreases.

A goal of this study was to provide guidance on optimal reconstruction method and dose calculation method for post- TARE ^{90}Y PET image based dosimetry. In order to expand the impacts of this research, OSEM reconstruction methods were included for those institutions that do not have the capabilities of GE imaging based Q. Clear methods. We assume that the Q.Clear method is the closest to ideal since it can be proven to mathematically converge[24]. Dose distributions resulting from OSEM 24 image reconstruction were statistically the same as those derived from Q. Clear $\beta = 1000$ based on dose profiles, maximum dose value and DVH curves.

When comparing our dose algorithm, WFBH, to MIRD we found them to be statistically equivalent. The difference between the two algorithms is the scattering kernel used. WFBH uses a $5 \times 5 \times 5$ kernel whereas the MIRD algorithm uses a $3 \times 3 \times 3$ kernel. At this level the extra voxels are negligible in its effect on dosimetry. Considering the maximum penetration depth for ^{90}Y is 11 mm with an average of 2.5 mm, it is expected that this expanded scattering kernel would not have a significant effect on the resulting dose distributions [1–3]. Our images have a 3 mm cubic voxel size so considering 3 voxels out from that point versus 5 voxels would be a matter of 9 mm compared to 15 mm respectively. Both of which are well above the average range.

According to Pasciak et al. the main contributing factor to differences in image based dosimetry from mathematical solutions is the image noise in a ^{90}Y PET/CT scan and less so the dose calculation algorithm when comparing LDM and dose-point kernel (DPK) algorithms [23]. Additionally, Pasciak et al. concluded through their studies that LDM appears to offer a slight improvement in accuracy compared to DPK when emissions scans are obtained on a PET system with a point spread function (PSF) greater than 3.25 mm at full width at half maximum (FWHM) along with a small voxel size but, in other situations depending on resolution and PSF, LDM leads to equal or greater error [23]. This study demonstrates that the LDM dose algorithm is highly dependent on reconstruction method. When looking at max dose values and DVH curves obtained via MIRD dose algorithms, there are very minimal differences from one reconstructed image to the next whereas with the LDM algorithm the differences are statistically larger. The realization that such subtle changes in the emission scan reconstruction can lead

to such large dose value changes is less than ideal for image based dosimetry post-TARE. Moreover, LDM dose algorithms were overestimating high dose regions and underestimating low dose regions. We found that across all six reconstruction methods, LDM would consistently give significantly higher max dose values than MIRD except for Q. Clear 7000 (data not shown). However, this is explained by the main differentiating assumption between the two algorithms. LDM calculates a dose for a given voxel based on the assumption that all of the energy is locally deposited within that one voxel, for a given decay event [23]. Whereas with convolution algorithms, specifically MIRD in this study, the dose value that is calculated considers the neighboring voxels based on the scattering kernel, i.e. not all of the energy is deposited strictly in that one given voxel. Thus, it would be expected that max dose values calculated using LDM would be higher than values obtained through MIRD due to the confinement of deposited energy. The agreement in max dose values between the two algorithms we saw with the Q. Clear 7000 reconstruction method is due to the over smoothing in that reconstructed image which is essentially forcing the activity to spread out across multiple voxels. Thus, the LDM dose algorithm was unintentionally applying the spread of activity between voxels as with the MIRD dose algorithm.

Conclusion

The use of ^{90}Y PET imaging post-TARE has the ability to identify dosimetric treatment success much sooner than historically where the lack of a successful treatment would not be apparent until follow-up appointments weeks to months after treatment [22]. The overall goal of this study was to advise on the optimal post-TARE ^{90}Y PET/CT image based dosimetry protocol. The convergence of the Q. Clear method has been proven[24] but we have been able to show comparable dosimetry resulting via OSEM image reconstruction, making it a valuable option to those who do not have a GE system. Overall, the most realistic and resistant to noise post-TARE image based dosimetry appears to be calculated via Q. Clear 1000 and OSEM 3 iterations and 24 subsets reconstruction algorithms with a convolution voxel based dose algorithm such as the SurePlan™ MIRD dose calculation algorithm explored in this paper. We recommend ^{90}Y activity distribution to be scaled based on the local clinic's obtain recovered activity fraction in the 37 mm diameter sphere until more sophisticated corrections are determined.

Abbreviations

TARE
Transarterial Radioembolization
^{90}Y
Yttrium-90
^{99m}Tc-MAA
Technetium-99m macroaggregated albumin particles
SPECT
single-photon emission computed tomography
PET

positron emission tomography
^{90}Zr
Zirconium-90
Q.Clear
Bayesian penalized likelihood, Regularized Reconstruction iterative algorithm
OSEM
Ordered Subsets Expectation Maximization
PET/CT
positron emission tomography/computed tomography
SPECT/CT
single photon emission computed tomography/computed tomography
LDM
SurePlan™ Local Deposition Method
MIRD
SurePlan™ Medical Internal Radiation Dose using voxel S values, 3 × 3 × 3 voxel kernel.
WFBH
dose convolution algorithm using voxel S values, 5 × 5 × 5 voxel dose kernel
DVH
dose volume histogram
WFBH Bkgrd
WFBH dose algorithm with mean background activity subtracted
RA
recovered activity
DPK
dose-point kernel
FWHM
full width at half maximum
VOI
value in the volume of interest

Declarations

Ethics approval

This research study was conducted retrospectively from data obtained for clinical purposes. We consulted extensively with the IRB of Wake Forest Baptist Health who determined that our study did not need ethical approval. An IRB official waiver of ethical approval was granted from the IRB of Wake Forest Baptist Health.

Consent to participate: Informed consent was waived by the IRB of WFBH.

Consent for publication: Informed consent was waived by the IRB of WFBH.

Availability of data and material: The datasets generated during and/or analyzed during the current study are available from the corresponding author on reasonable request.

Competing interests: BCT declares no conflict of or competing interests. WAD serves as an advisory board consultant for Sirtex Medical.

Funding: Not applicable

Authors' contributions: Both authors contributed to the conception, design and analysis of the study. Data collection was performed by BCT. First draft of the manuscript was written by BCT and WAD commented and edited on each version of the manuscript. Both authors read and approved the final manuscript.

Acknowledgements: We would like to thank Dorsey Faught and Will Cork with their help and contributions with MIM workflow creation.

References

1. Dezarn WA, Cessna JT, DeWerd LA, Feng W, Gates VL, Halama J, et al. Recommendations of the American Association of Physicists in Medicine on dosimetry, imaging, and quality assurance procedures for 90Y microsphere brachytherapy in the treatment of hepatic malignancies. Med Phys. 2011;38:4824–45.
2. Kennedy A, Nag S, Salem R, Murthy R, McEwan AJ, Nutting C, et al. Recommendations for Radioembolization of Hepatic Malignancies Using Yttrium-90 Microsphere Brachytherapy: A Consensus Panel Report from the Radioembolization Brachytherapy Oncology Consortium. Int J Radiat Oncol. 2007;68:13–23.
3. Tong AKT, Kao YH, Too CW, Chin KFW, Ng DCE, Chow PKH. Yttrium-90 hepatic radioembolization: clinical review and current techniques in interventional radiology and personalized dosimetry. Br J Radiol The British Institute of Radiology. 2016;89:20150943.
4. Garin E, Rolland Y, Laffont S, Edeline J. Clinical impact of 99mTc-MAA SPECT/CT-based dosimetry in the radioembolization of liver malignancies with 90Y-loaded microspheres. Eur J Nucl Med Mol Imaging. 2016;43:559–75.
5. Song YS, Paeng JC, Kim H-C, Chung JW, Cheon GJ, Chung J-K, et al. PET/CT-Based Dosimetry in 90Y-Microsphere Selective Internal Radiation Therapy: Single Cohort Comparison With Pretreatment Planning on 99mTc-MAA Imaging and Correlation With Treatment Efficacy. Medicine (Baltimore) [Internet]. 2015 [cited 2020 Jul 23];94. Available from: https://www.ncbi.nlm.nih.gov/pmc/articles/PMC4616469/.
6. Kafrouni M, Allimant C, Fourcade M, Vauclin S, Guiu B, Mariano-Goulart D, et al. Analysis of differences between 99mTc-MAA SPECT- and 90Y-microsphere PET-based dosimetry for hepatocellular carcinoma selective internal radiation therapy. EJNMMI Res. 2019;9:62.

7. Knešaurek K, Machac J, Muzinic M, DaCosta M, Zhang Z, Heiba S. Quantitative Comparison of Yttrium-90 (90 Y)-Microspheres and Technetium-99m (99 m Tc)-Macroaggregated Albumin SPECT Images for Planning 90 Y Therapy of Liver Cancer. Technol Cancer Res Treat. SAGE Publications Inc; 2010;9:253–61.
8. Tafti BA, Padia SA. Dosimetry of Y-90 Microspheres Utilizing Tc-99m SPECT and Y-90 PET. Semin Nucl Med. 2019;49:211–7.
9. Wondergem M, Smits MLJ, Elschot M, de Jong HWAM, Verkooijen HM, van den Bosch MAAJ, et al. 99mTc-macroaggregated albumin poorly predicts the intrahepatic distribution of 90Y resin microspheres in hepatic radioembolization. J Nucl Med Off Publ Soc Nucl Med. 2013;54:1294–301.
10. Scott NP, McGowan DR. Optimising quantitative 90Y PET imaging: an investigation into the effects of scan length and Bayesian penalised likelihood reconstruction. EJNMMI Res. 2019;9:40.
11. Jiang M, Fischman A, Nowakowski FS. Segmental Perfusion Differences on Paired Tc-99m Macroaggregated Albumin (MAA) Hepatic Perfusion Imaging and Yttrium-90 (Y-90) Bremsstrahlung Imaging Studies in SIR-Sphere Radioembolization: Associations with Angiography. J Nucl Med Radiat Ther [Internet]. 2012 [cited 2020 Jun 25];03. Available from: https://www.omicsonline.org/segmental-perfusion-differences-on-paired-tc-99m-macroaggregated-albumin-maa-hepatic-perfusion-imaging-and-yttrium-90-y-90-bremsstrahlung-imaging-studies-in-sir-sphere-2155-9619.1000122.php?aid=4711.
12. Rowley LM, Bradley KM, Boardman P, Hallam A, McGowan DR. Optimization of Image Reconstruction for 90Y Selective Internal Radiotherapy on a Lutetium Yttrium Orthosilicate PET/CT System Using a Bayesian Penalized Likelihood Reconstruction Algorithm. J Nucl Med. 2017;58:658–64.
13. Elschot M, Vermolen BJ, Lam MGEH, Keizer B de, Bosch MAAJ van den, Jong HWAM de. Quantitative Comparison of PET and Bremsstrahlung SPECT for Imaging the In Vivo Yttrium-90 Microsphere Distribution after Liver Radioembolization. PLOS ONE. Public Library of Science; 2013;8:e55742.
14. D'arienzo M. Emission of β + Particles Via Internal Pair Production in the 0+ – 0 + Transition of 90Zr: Historical Background and Current Applications in Nuclear Medicine Imaging. Atoms. 2013;1:2–12.
15. Selwyn RG, Nickles RJ, Thomadsen BR, DeWerd LA, Micka JA. A new internal pair production branching ratio of 90Y: The development of a non-destructive assay for 90Y and 90Sr. Appl Radiat Isot. 2007;65:318–27.
16. Bé M, -m, Chisté V, Dulieu C, Browne E, Baglin C, Chechev V, et al. Monographie BIPM-5 Table of Radionuclides. 2006.
17. Willowson K, Forwood N, Jakoby BW, Smith AM, Bailey DL. Quantitative (90)Y image reconstruction in PET. Med Phys. 2012;39:7153–9.
18. D'Arienzo M, Chiaramida P, Chiacchiararelli L, Coniglio A, Cianni R, Salvatori R, et al. 90Y PET-based dosimetry after selective internal radiotherapy treatments. Nucl Med Commun. 2012;33:633–40.
19. Lhommel R, van Elmbt L, Goffette P, Van den Eynde M, Jamar F, Pauwels S, et al. Feasibility of 90Y TOF PET-based dosimetry in liver metastasis therapy using SIR-Spheres. Eur J Nucl Med Mol Imaging. 2010;37:1654–62.

20. Kao Y-H, Steinberg JD, Tay Y-S, Lim GK, Yan J, Townsend DW, et al. Post-radioembolization yttrium-90 PET/CT - part 2: dose-response and tumor predictive dosimetry for resin microspheres. EJNMMI Res. 2013;3:57.
21. Chang TT, Bourgeois AC, Balius AM, Pasciak AS. Treatment Modification of Yttrium-90 Radioembolization Based on Quantitative Positron Emission Tomography/CT Imaging. J Vasc Interv Radiol. 2013;24:333–7.
22. 10.3389/fonc.2014.00038/full
Pasciak AS, Bourgeois AC, McKinney JM, Chang TT, Osborne DR, Acuff SN, et al. Radioembolization and the Dynamic Role of 90Y PET/CT. Front Oncol [Internet]. 2014 [cited 2019 Jun 24];4. Available from: https://www.frontiersin.org/articles/10.3389/fonc.2014.00038/full.
23. Pasciak AS, Bourgeois AC, Bradley YC. A Comparison of Techniques for 90Y PET/CT Image-Based Dosimetry Following Radioembolization with Resin Microspheres. Front Oncol [Internet]. 2014 [cited 2020 Jun 9];4. Available from: https://www.ncbi.nlm.nih.gov/pmc/articles/PMC4033229/.
24. Ross S QClear [Internet]. GE Healthcare; 2014 p. 9. Available from: https://www.gehealthcare.com.au/-/jssmedia/739d885baa59485aaef5ac0e0eeb44a4.pdf.
25. Low DA, Harms WB, Mutic S, Purdy JA. A technique for the quantitative evaluation of dose distributions. Med Phys. 1998;25:656–61.
26. Gnesin S, Kieffer C, Zeimpekis K, Papazyan J-P, Guignard R, Prior JO, et al. Phantom-based image quality assessment of clinical 18F-FDG protocols in digital PET/CT and comparison to conventional PMT-based PET/CT. EJNMMI Phys. 2020;7:1.

Figures

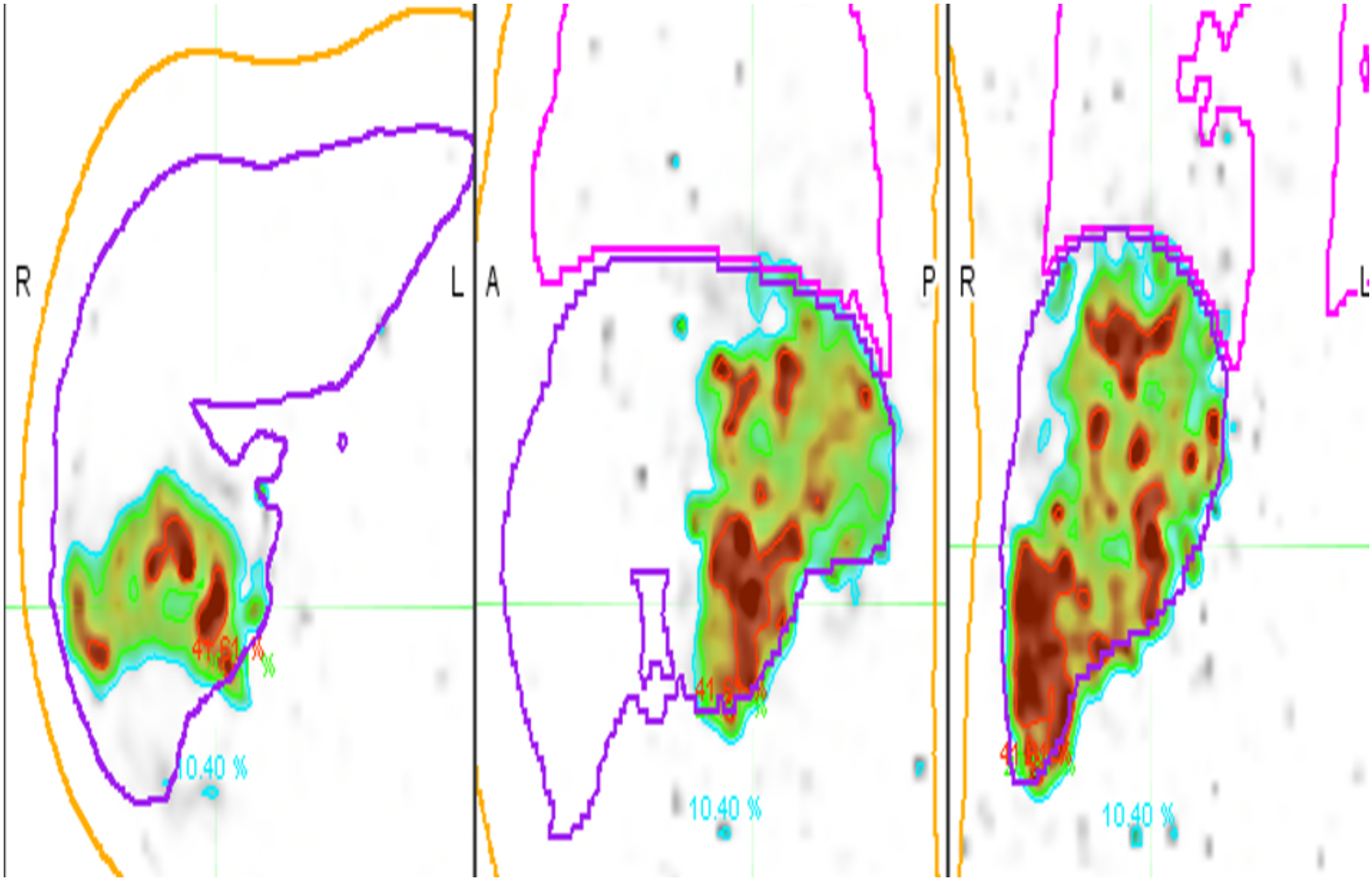

Figure 1

Representative dose distribution PET image showing SurePlanTM MIRD dose distribution with Q.Clear 1000. The whole body is contoured in orange, liver in purple and lungs in pink. Red denotes 100 Gy, green is 50 Gy and blue is 25 Gy

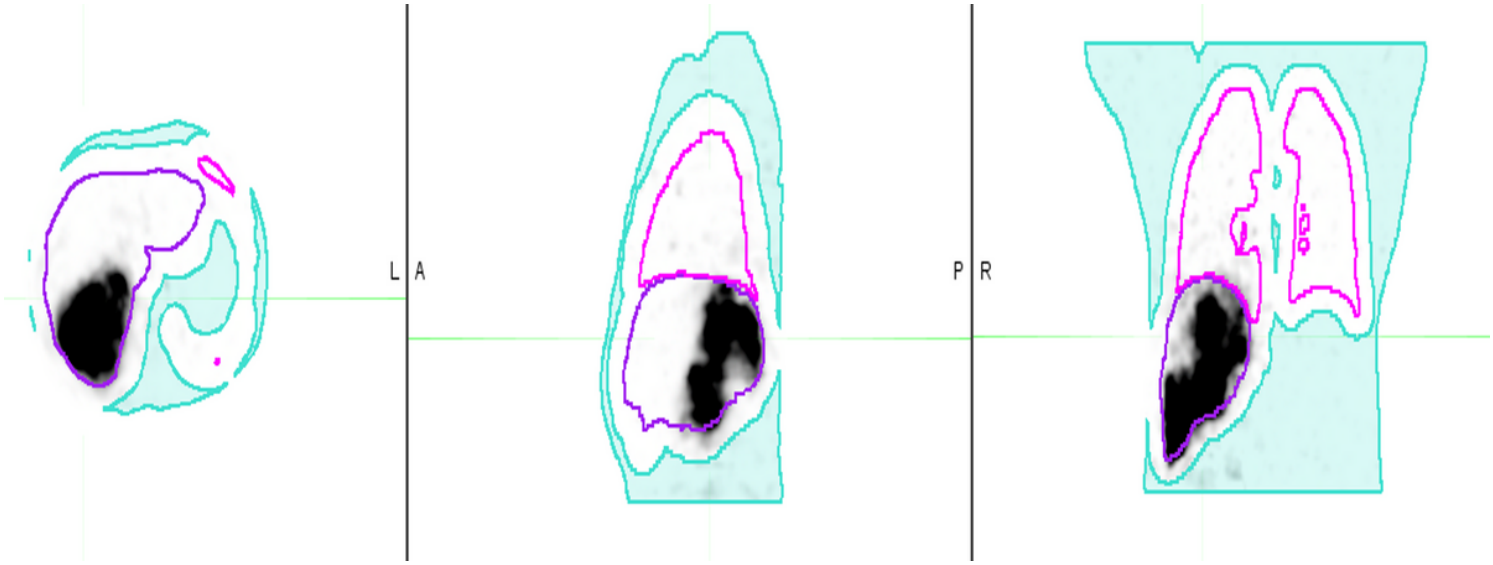

Figure 2

Definition of background contour Representative PET image showing the background contour shaded in blue, liver in purple and lungs in pink.

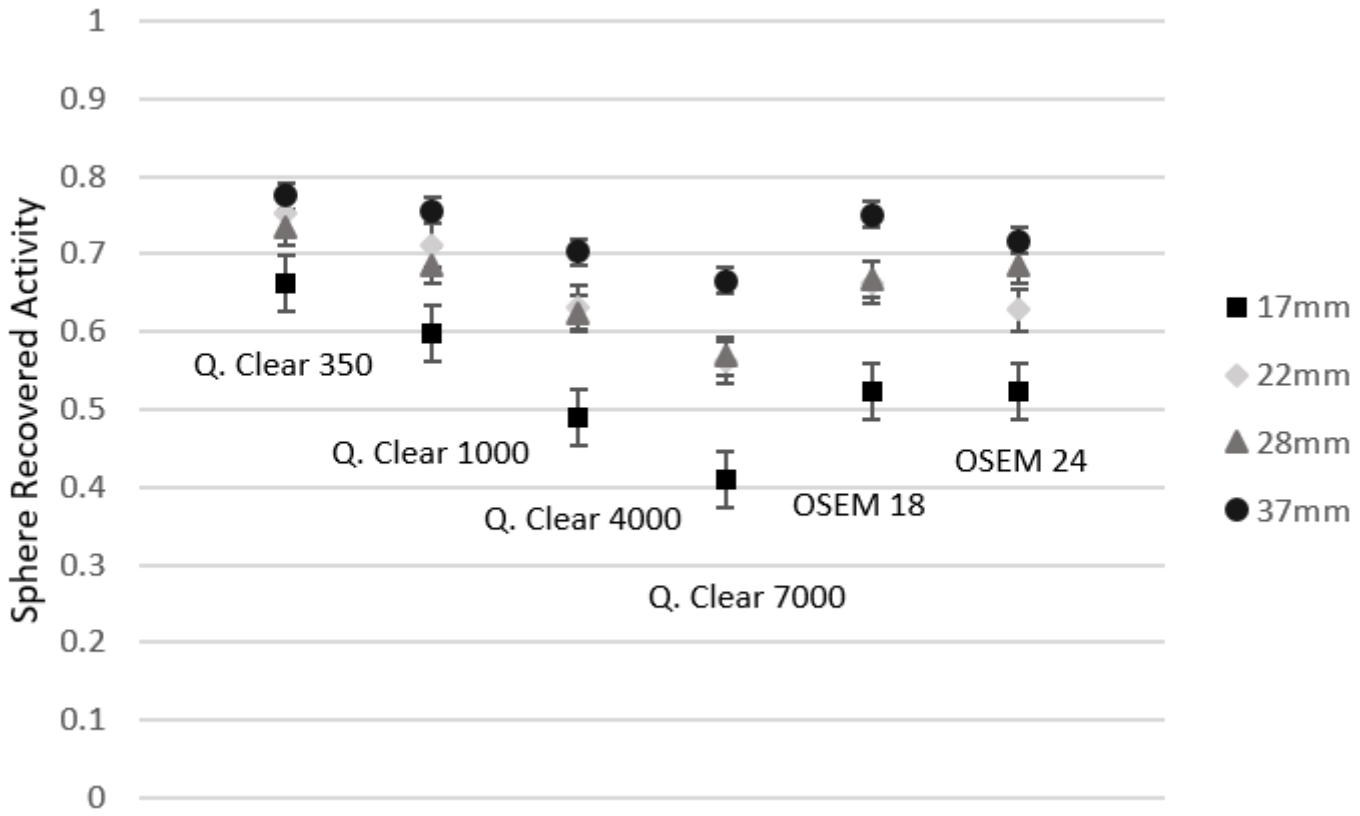

Figure 3

Recovered activity values grouped by reconstruction method Calculated recovered activity for each sphere size in the phantom is shown with one standard deviation error bars. As β value increases the recovered activity accuracy decreases.

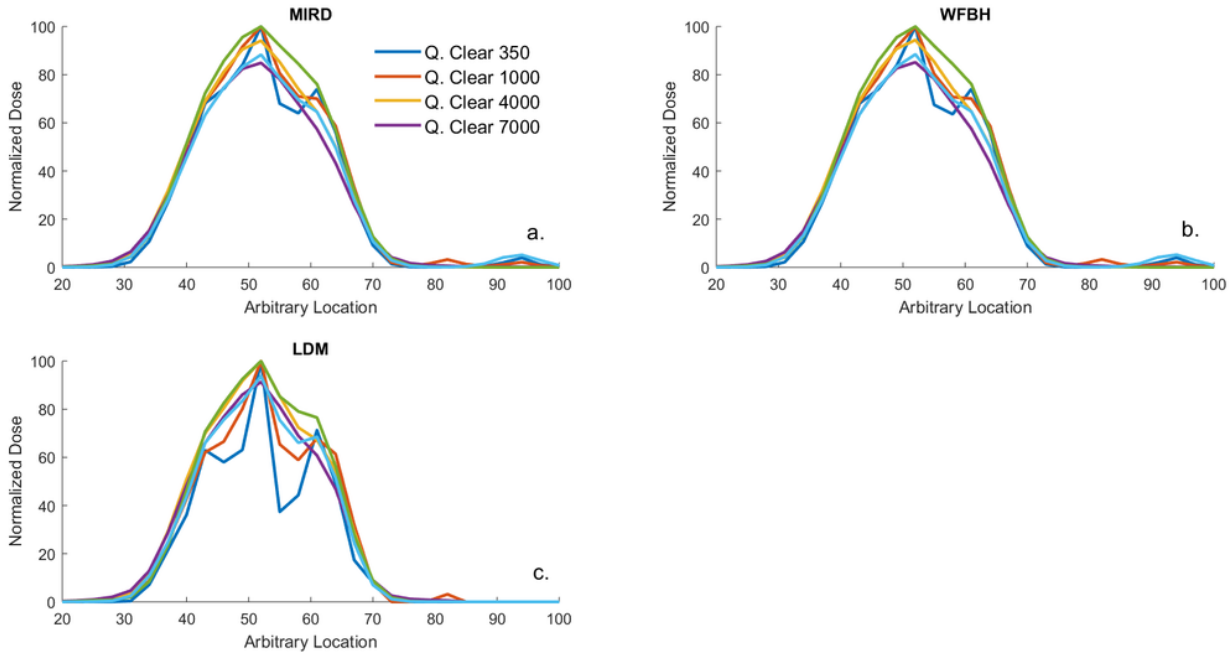

Figure 4

Dose profiles based on emission image of phantom Normalized dose profiles based on each dose calculation algorithm are shown for each of the Q. Clear reconstruction method variations. Fig 4a shows dose distributions based on MIRD, Fig 4b based on WFBH and Fig 4c based on LDM. Fig 4c shows the more drastic difference in dose value as you go from voxel to voxel.

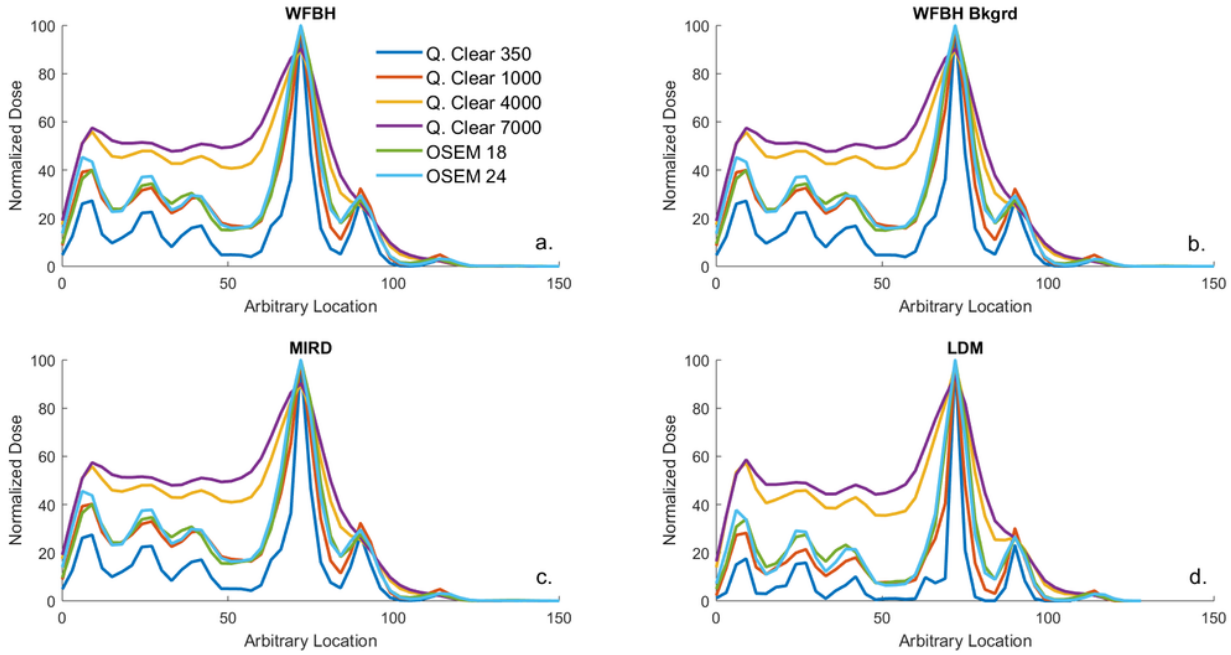

Figure 5

Dose profiles based on post-TARE 90Y PET These dose profiles are based on a sagittal cut through the max dose point defined by the dose distribution created using MIRD Q. Clear 1000. Fig 5a is based on WFBH dose method, Fig 5b is based on WFBH Bkgrd, Fig 5c is based on MIRD and Fig 5d on LDM.

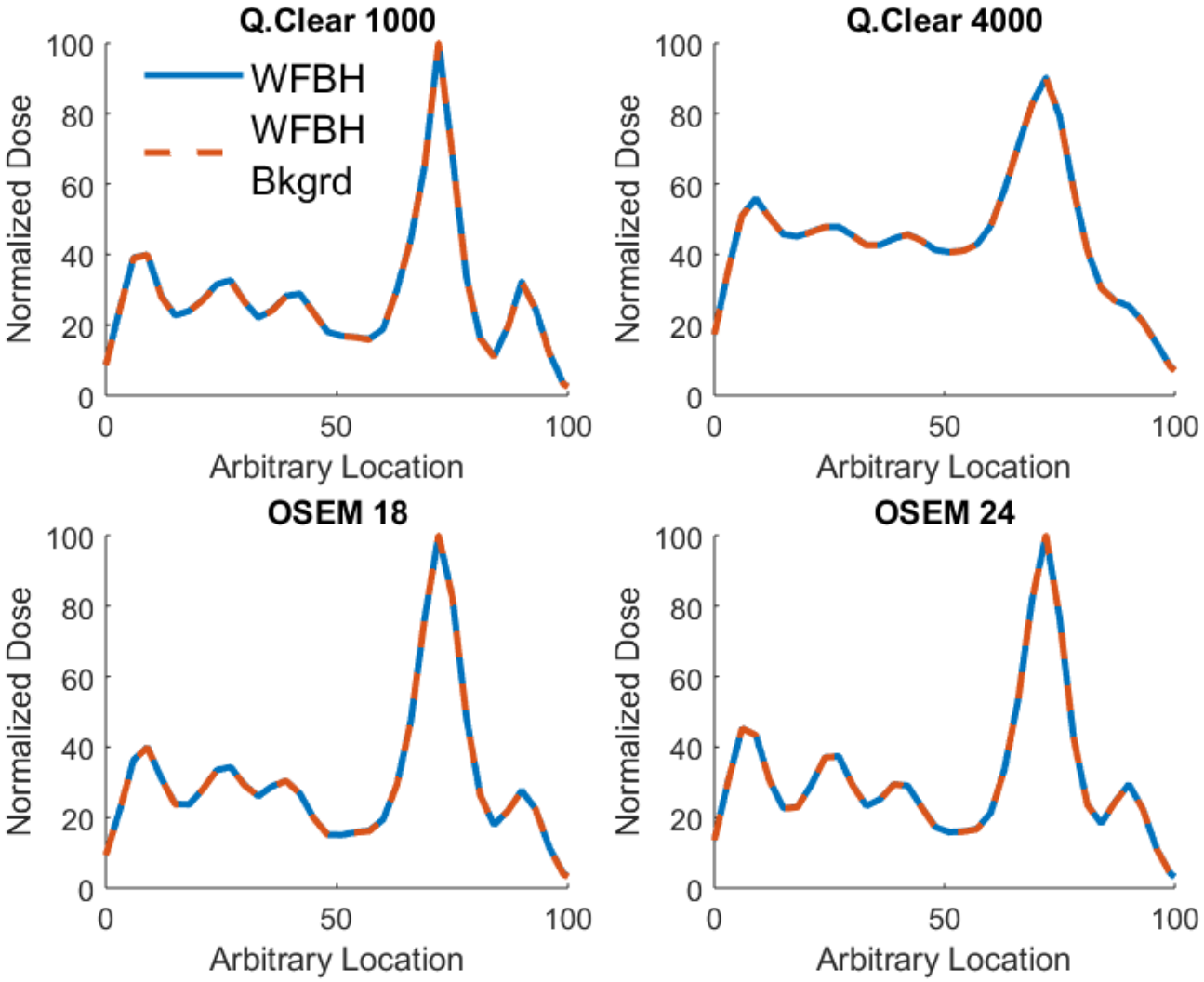

Figure 6

Comparison of WFBH and WFBH Bkgrd dose profiles Sagittal cut through the max dose point defined by the dose distribution created using MIRD Q. Clear 1000 showing the dose profiles for WFBH and WFBH Bkgrd dose algorithms. Note the overlap of the two helping to support that these dose distributions are not different.

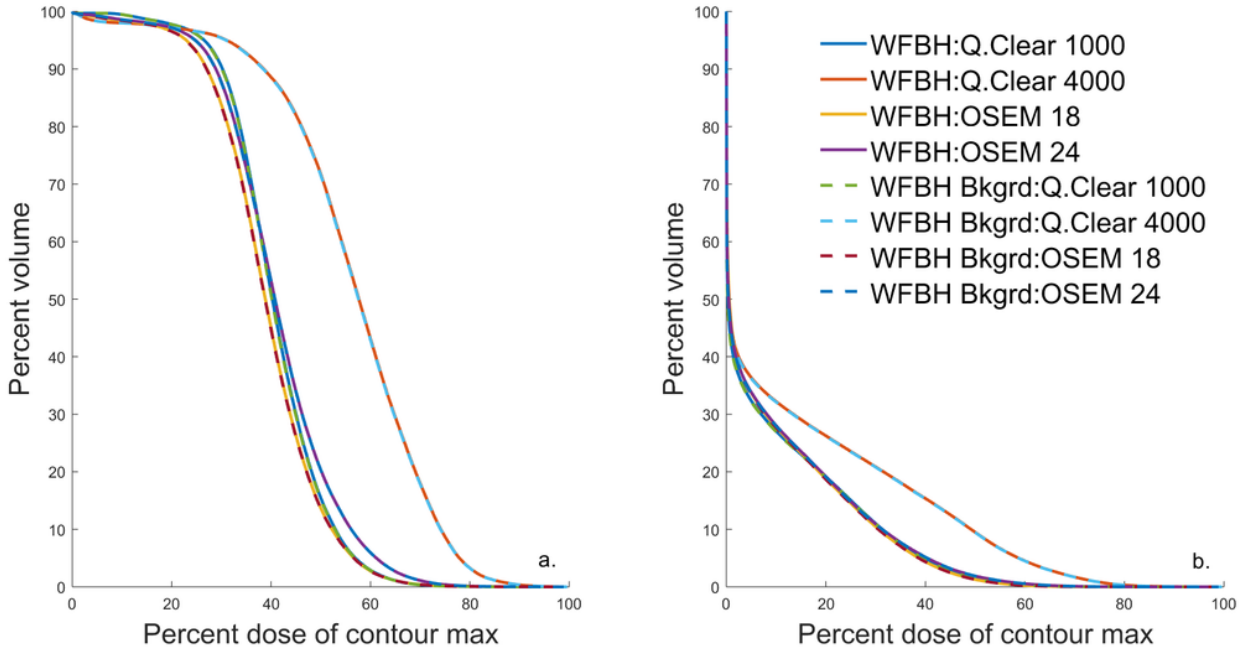

Figure 7

7 DVH curves comparing WFBH and WFBH Bkgrd dose methods Fig 7a is a representative DVH curve for the treated area and shows the similarities of these two dose algorithms. Fig 7b is the representative DVH curve for the liver. Once again these two dose algorithms give the same curves adding to the argument that background subtraction is sufficiently handled within the reconstruction methods.

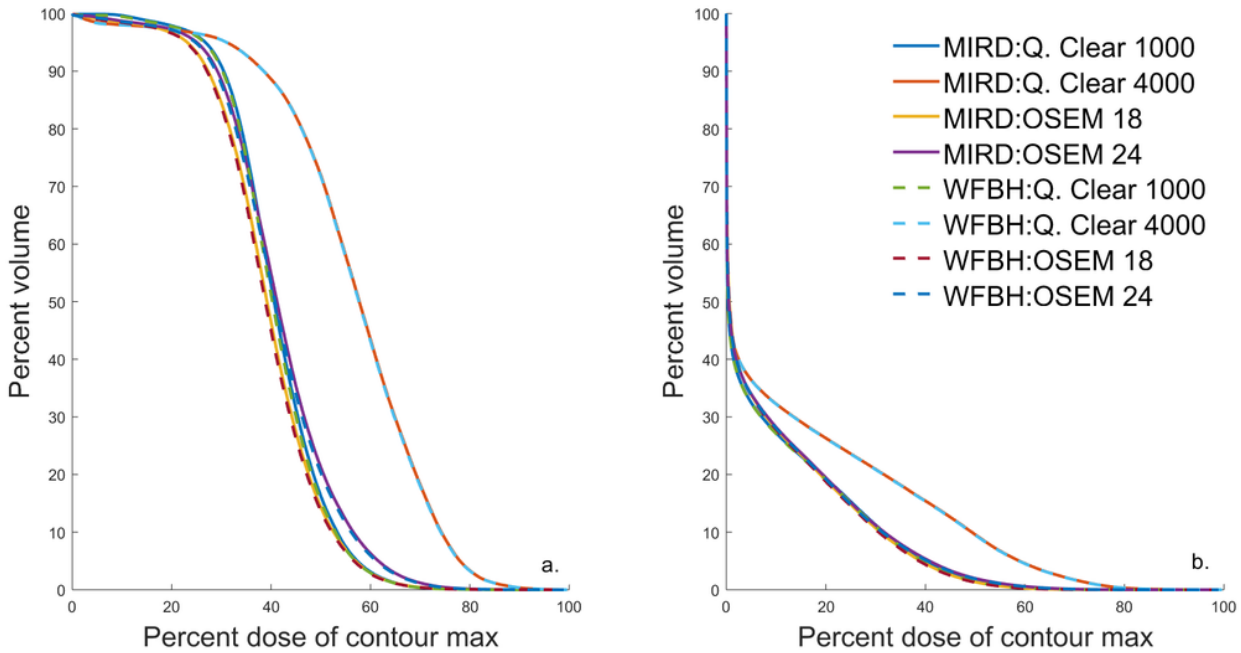

Figure 8

DVH curves comparing MIRD and WFBH dose methods Fig 8a is a representative DVH curve for the treated which shows the similarities in WFBH and MIRD dose calculation algorithms. Fig 8b is the representative DVH curve for the liver. In both contours, the outlier DVH curves are based on the Q. Clear 4000 reconstruction method.

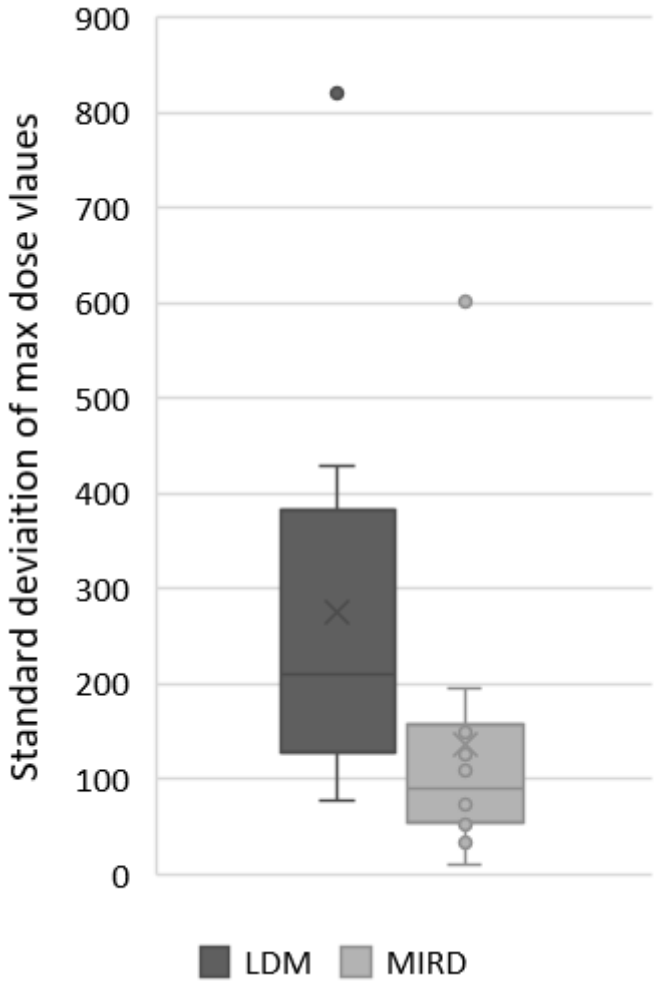

Figure 9

Maximum dose values based on dose algorithm The spread in standard deviation of the maximum dose value across each reconstruction method for each patient is shown. LDM gives a higher variation in max dose values from one reconstruction method to the next.

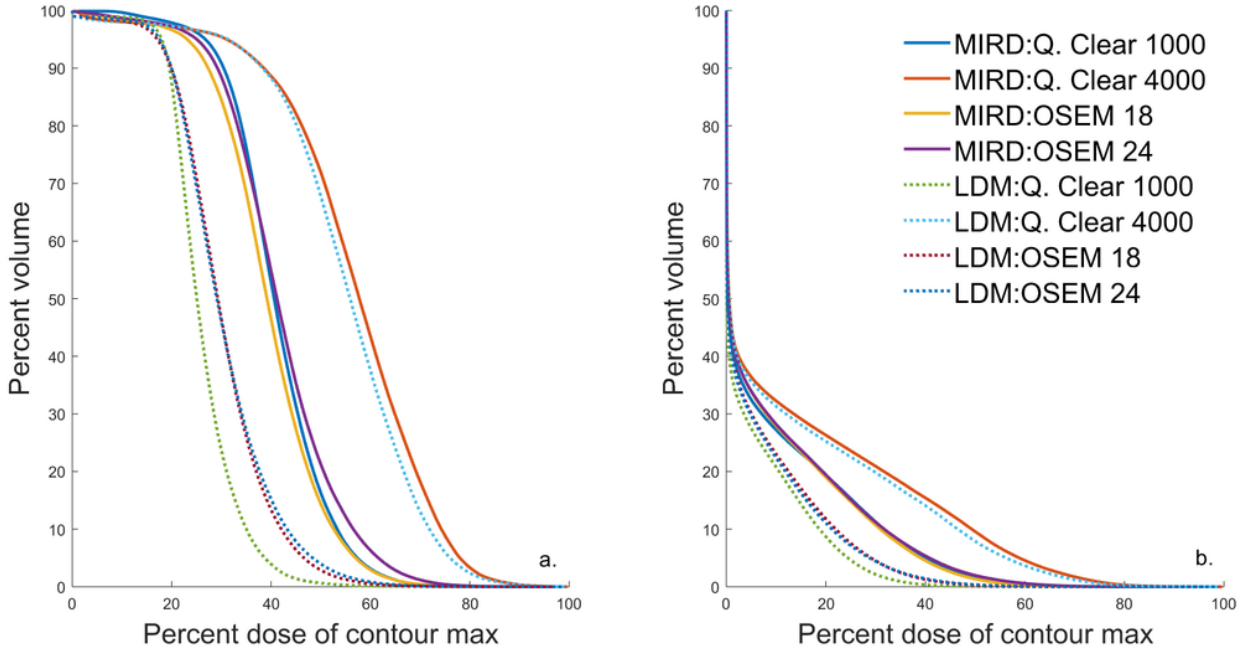

Figure 10

DVH curves comparing MIRD and LDM dose methods Fig 10a is a representative DVH curve for the treated region whereas Fig 10b are DVH curves for the liver contour. LDM dose algorithms cause the curve to be shifted to the left of the MIRD algorithm. It should be noted the x-axis is based on percent dose of the contour max to try to eliminate the differences in max dose value and instead can look at the distribution of delivered dose.

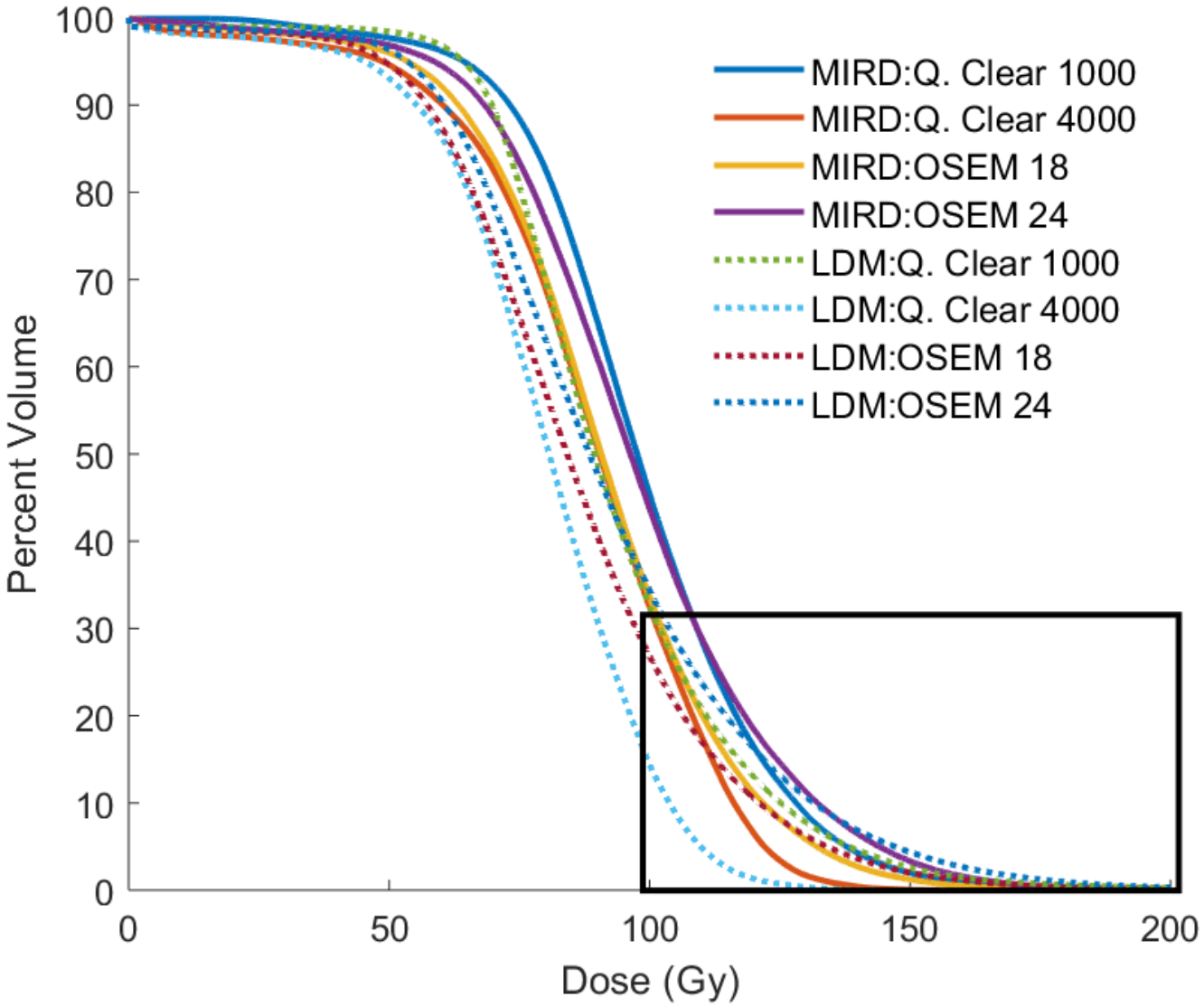

Figure 11

Absolute dose DVH curves for treated region Representative DVH curve for the treated region with absolute dose on the x-axis. Note the crossing over of LDM DVH curves within the box showing the algorithm's tendency to have higher dose than MIRD methods.